

Optical constants and absorption properties of Te and TeO thin films in the 13-14 nm spectral range

LUIS V. RODRÍGUEZ-DE MARCOS,^{1,5} SHENBAGA M. P. KALAISELVI,²
ONG BIN LEONG,³ PRANAB K. DAS,² MARK B. H. BREESE,^{2,3,4}
AND ANDRIVO RUSYDI^{2,3,4,6}

¹NASA Goddard Space Flight Center & Catholic University of America (CRESST II Program), mail code 665, Greenbelt, MD 20771, USA

²Singapore Synchrotron Light Source, National University of Singapore, 5 Research Link, 117603, Singapore

³Physics Department, National University of Singapore, 2 Science Drive 3, 117542, Singapore

⁴NUSNNI-NanoCore, National University of Singapore, Singapore 117411, Singapore

⁵luis.v.rodriguezdemarcos@nasa.gov

⁶phyandri@nus.edu.sg

Abstract: Undesired mask-induced effects caused by thick absorber layers in EUV photomasks reduce the quality of the projected patterns at the wafer stage in EUV photolithography scanners. New materials with better absorption properties than the state-of-the-art absorbers, TaN and TaBN, are required to mitigate these effects. In this work, we investigated the optical properties (δ and k) of Te and TeO films in the 13-14 nm range, and the absorption properties of these two materials at 13.5 nm. δ and k are obtained through fitting experimental values of reflectivity versus angle of incidence in the EUV range. We follow a methodology which combines different characterization techniques (X-ray reflectivity, EUV reflectivity, and X-ray photoemission spectroscopy) to reduce the number of free parameters in models and hence, increase the reliability of the optical constants obtained. At 13.5 nm, we obtain $\delta=0.03120$, $k = 0.07338$ for Te, and $\delta=0.04099$, $k = 0.06555$ for TeO. To experimentally verify the absorption properties of these materials, different thicknesses of Te and TeO films are cast on top of a state-of-the-art mask-quality EUV multilayer with 66.7% reflectivity at 13.5 nm. We found that a reflectivity of $\sim 0.7\%$ can be attained with either 32.4 nm of Te, or 34.7 nm of TeO, greatly surpassing the absorption properties of TaN and TaBN. The morphology and surface roughness of the Te and TeO films deposited on the multilayer are also investigated.

© 2020 Optical Society of America under the terms of the [OSA Open Access Publishing Agreement](#)

1. Introduction

Extreme Ultraviolet Lithography (EUVL) operating at 13.5 nm is on the verge of becoming competitive. Recently several EUV scanners, qualified to deliver high production volumes with a good uptime operation, have been installed in semiconductor foundries facilities. This advanced lithographic technology will take a leading role in patterning semiconductor devices at the 7 nm node, and beyond. Now that most of the earlier technology-stopping problems have been solved, there are still few remaining issues which it is necessary to address in order to increase the throughput and/or the quality of the printed integrated circuits. One of them is the shadowing effect produced by thick absorbers in EUV photomasks when illuminated at oblique incidence (6 degrees from normal incidence). In photomasks, absorbers are patterned based on a given chip design. The purpose of absorbers is to reduce the reflectivity of the underlying reflective multilayer (ML) and hence, create reflectivity contrast. Patterned thick absorbers cause undesired geometric shadows which are propagated through the reflective optics onto the wafer,

thus affecting the quality of the printed patterns (for instance, by shifting). A comprehensive analysis of mask effects caused by thick absorbers can be found in reference [1]. The utilization of alternative materials with higher extinction coefficient, k , would considerably reduce the required absorber thickness and hence, minimize the mask effects. Additionally, the utilization of absorbers with the real part of the refractive index ($\delta=1-n$) close to 0 minimizes the undesired phase jump in the reflected wavefront at the absorber edges produced by the index contrast between the free space and the patterned absorber. Fig. 4 in reference [2] neatly summarizes these two effects. TaN and TaBN are the state-of-the-art absorbers for EUVL masks. [3] They present good optical properties at 13.5 nm, along with other valuable properties (mechanical, chemical and morphological). However, the typical TaN thickness required to attain a reflectivity of less than 2% is ~ 50 -60 nm, which causes mask shadowing effects. Additionally, δ of both TaN and TaBN significantly differ from 0 at 13.5 nm, which is also undesired.

Figure 1 shows a δ , k diagram of selected materials with good absorbing properties at 13.5 nm. The displayed δ , k values are either found in the literature or calculated from their respective atomic scattering factors [4] using nominal densities. Each orange arrow in Fig. 1 indicates the direction which the complex refractive index of an ideal absorber should follow to mitigate shadow effect or phase shifts in the reflected wavefront. Aside from TaN and TaBN, several materials (including oxides, nitrides, and alloys) shown in Fig. 1 have been studied as absorbers: SnO, [5] Ni, Co, Ni-Al, [6] Ta, Cr, TiN, Ti, Al, Al-Cu. [7] An absorber-based multilayer stack NiPt/TiN [8] has been also proposed as absorber. Alternative architectures to absorber-capped ML stacks, such as patterned reflectors, [9] have been also proposed. However, in terms of optical properties at 13.5 nm, Tellurium and its oxides are good candidates [10] to replace TaN and TaBN, as is highlighted in Fig. 1. The high values of k of Te-based materials are attributed to the presence of the Te $N_{2,3}$ strong absorption edge peaked at ~ 15 nm. Hence, Te-alloys as PtTe and TaTe₂, [11] as well as oxides of Te-alloys such as TaTe₂O₇ [12] have been already investigated, yielding refractive indexes at 13.5 nm of ($\delta=0.0660$, $k=0.0763$), ($\delta=0.0249$, $k=0.0488$) and ($\delta=0.0471$, $k=0.0555$), respectively. These materials are also displayed in Fig. 1. In this work we investigate the optical properties of Te and TeO in the 13-14 nm range, and their absorbing capabilities. Even though in Fig. 1 we show optical constants of Te and TeO films, these values

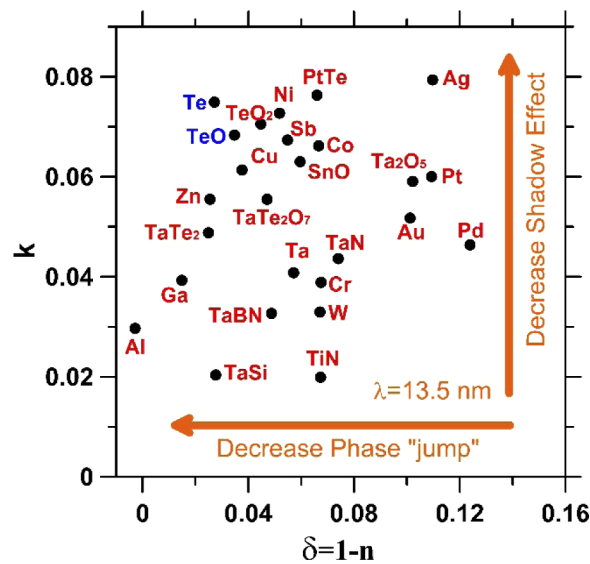


Fig. 1. δ , k diagram for several materials at 13.5 nm. The materials studied in this work are highlighted in blue.

are calculated from the atomic scattering factors under the independent atom approximation. This model yields inaccurate values in the proximity of absorption edges, where the interaction between atoms cannot be neglected. [13] Hence, a significant difference between the calculated δ , k using atomic scattering factors and the real values is expected. It must be pointed out that alternative materials intended to replace TaN or TaBN need to satisfy other important requirements aside from their good absorption properties. These additional requirements are: morphology (amorphous or fine grain), low surface roughness, low stress, good adhesion to Ru cap layer, stability over time, compatibility with standard mask cleaning chemistries, have a good deep ultraviolet contrast with ML for defect inspection, etchable in common RIE chemistries with high pattern fidelity, and good etching rate and selectivity with standard capping layers. [6,7] In this work we have only analyzed the optical properties. This manuscript is organized as follows: Section 2 describes the thin film deposition system and the characterization set up. Section 3 details the procedure followed to calculate the optical constants of Te and TeO thin films in the 13-14 nm range. The absorbing properties and morphology of the later materials deposited on EUV MLs are analyzed in section 4.

2. Experimental set up and measurements

Te and TeO samples were deposited with pulsed laser deposition system (PLD) at the Singapore Synchrotron Light Source (SSLS); the PLD system is an integrated component of the SUV beamline. [14] The PLD deposition chamber was pumped by turbo molecular and diaphragm pumps; in order to accelerate degassing, deposition chamber was baked out up to $\sim 150^{\circ}\text{C}$ for 4 days before deposition. Base pressure was $8 \cdot 10^{-9}$ Torr. A Te target of 99.999% purity from LATECH was ablated with a solid-state laser operating at 266 nm, with pulse frequencies of 10 Hz and laser power output of 100 mJ/mm^2 . The angle of incidence of the laser on target was 45° , and the target-to-substrate distance was ~ 100 mm. Target rastering and rotation were used to uniformly ablate the entire target surface. Before deposition, Te target was pre-ablated to remove surface contaminants and oxides. For optical constants determination, Te and TeO thin films were deposited on $10 \text{ mm} \times 10 \text{ mm} \times 1 \text{ mm}$ double-side polished Quartz substrates from LATECH, with a surface roughness of less than 3 \AA . Substrates rotated during deposition at $\sim 29 \text{ deg/s}$. Films were deposited at room temperature. Deposition of TeO was made by ablating Te in an O_2 partial pressure of 10 mTorr, which was selected by a mass flow controller. Film thicknesses were controlled as a function of number of laser shots, which were previously calibrated through grazing incidence X-ray reflectivity (XRR). EUV reflectivity measurements in the 13-14 nm range were carried out at SINS-EUV Branch beamline at SSLS. The beamline is optimized for multilayer reflectometry and optical constants characterization in the 5-25 nm range, covering the most critical portion of the EUV spectrum for mask blank reflectometry. A 130 l/mm grating was used during the measurements. Both monochromator entrance and exit slits were set to a width of $100 \mu\text{m}$. With this configuration, the resolving power $E/\Delta E$ is around 10^3 . Higher harmonic orders and stray light were suppressed by using a 300-nm thick self-standing Si transmission filter. Wavelength calibration is critical for EUV mask blank reflectometry. Hence, the monochromator is periodically calibrated at SINS end station by using X-ray Photoemission Spectroscopy (XPS) capabilities on a reference clean Au sample, with is always kept under UHV conditions. As the monochromator may accumulate errors during the scans, before each measurement a scan across the Si L_2 edge at $\sim 99.82 \text{ eV}$ is performed to correct any wavelength drift. The repeatability of the Si edge wavelength is within 5 pm. Reflectance repeatability is within 0.1%. Periodically a sample is measured both at the 6.3.2 beamline at The Center for X-ray Optics (CXRO) and at EUV branch at SSLS. If we assume that 6.3.2 is one well-known reference for EUV metrology, reflectivity measured with EUV branch beamline is systematically 1% lower than reflectivity on the same sample measured at CXRO; this 1% can be considered as a good relative error estimation. Data was collected with a Si photodiode detector, and all scans are

normalized with the drain current recorded on one of the beamline refocusing mirrors (M2). The base pressure of the end-station is $3 \cdot 10^{-8}$ Torr. Samples are loaded in the reflectometer through a load lock chamber. The XRR measurements were performed with the X-ray Diffractometry and Development (XDD) beamline at SSLS. Reflectivity measurements of samples in a θ - 2θ configuration were performed in the θ range between 0.2° and 2° with a step of $5 \cdot 10^{-4}$ degrees. The incident wavelength was set to 0.15406 nm by means of a Si crystal monochromator. The exit slit was set to 0.5 mm. Typical spectral resolution $E/\Delta E$ for this configuration is higher than 10^3 . Additional information about XDD beamline can be found in reference [15]. Stoichiometry and oxidation states of TeO films and of the native oxide on Te films were analysed by XPS. The XPS measurements were performed at the SUV beamline¹⁴. The data was collected using Scienta-Omicron DA30L electron analyzer in transmission-XPS mode. Laboratory Al $K\alpha$ X-ray (photon energy = 1486.6 eV) was used as photon source. Due to the insulating nature of film and substrate, sample charging effects were experienced during the photoemission measurements, and therefore a shift in the XPS peak positions with respect to their original positions was expected. Such effects have been considered during the data analysis. All measurements were performed at room temperature.

3. Data analysis and optical constants

The procedure for the refractive index (δ and k) characterization of TeO and Te thin films combines different characterization techniques (EUV reflectivity vs incident angle and vs wavelength, XPS, and XRR) to fix parameters beforehand, so that the final δ , k calculation will rely on a minimum number of free parameters. Combining different techniques will give more consistent optical constants than solitary unconstrained fitting of EUV reflectance as a function of angle. [16] Hence, prior to the analysis of Te and TeO samples deposited on quartz substrates, the reflectivity of a bare quartz substrate was measured at 75° , 60° , and 45° from normal incidence in the 13-14 nm range with a step of 0.1 nm. The purpose of this measurement was to model the substrate and to experimentally find the linear polarization degree of the upcoming beam at the end-station. A model for the substrate was built with IMD software. The substrate parameters which better matched the experimental data were a 1 mm SiO_2 layer, with optical constants from reference [17] (SiO_2 .nk file in IMD software), and a 10-Å thick sub-surface layer with a roughness of 3.5 Å, with optical constants of amorphous SiO_2 also from reference [17] (a- SiO_2 .nk file in IMD), and with a reduced real part of the refractive index of 99.2%. This index reduction may be explained because potential contaminants trapped on the surface, such hydrocarbons or water, might slightly decrease the refractive index of the subsurface; the possible effect of contaminants in k was ignored. The polarization degree was found to be 0.99 (using the criteria where +1 is pure s polarization and -1 is pure p polarization), which agrees with the typical values found in SINS beamline (EUV beamline is a branch of SINS). Even though the polarization degree is wavelength-dependent, we assumed a constant value across the 13-14 nm range. Fig. 2 displays the EUV reflectivity of a bare Quartz substrate at three angles of incidence along with the model for the substrate.

XPS measurements were performed to verify the stoichiometry of TeO and of the native oxide growth on Te, as it oxidizes when exposed to atmosphere. The strategy is that, if the XPS spectra taken from TeO and from the native oxide growth on Te samples are (fairly) similar, then in the optical models we could approximate the native oxide on Te with the optical constants of TeO. Fig. 3 shows the wide scans of the samples TeO and native oxide on Te. The core-level peaks found for both samples are assigned to Te, O and C. The spectra were charged-corrected to the unoxidized $\text{Te}3d_{5/2}$ core level peak at 573 eV. Fig. 4 shows the deconvolved $\text{Te}3d$ core-level spectra for samples TeO and native oxide on Te. In this plot, the two main peaks in the spectra correspond to the oxidized peaks of the doublet at 576.0 eV ($\text{Te}3d_{5/2}$) and 586.3 eV ($\text{Te}3d_{3/2}$), respectively. These peaks are attributed to the presence of Te oxide. The spectra for both samples

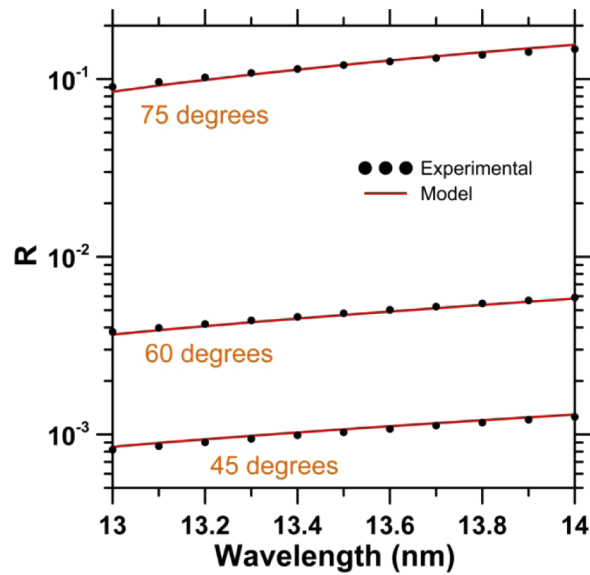


Fig. 2. Reflectivity measurements on a bare quartz substrate as a function of wavelength at three different angles of incidence, 45°, 60° and 75°, along with the model.

also indicate the presence of a small amount of unoxidized Te, identified by the presence of the unoxidized Te3d doublet at 573.0 eV ($\text{Te}3d_{5/2}$) and 583.1 eV ($\text{Te}3d_{3/2}$) respectively.

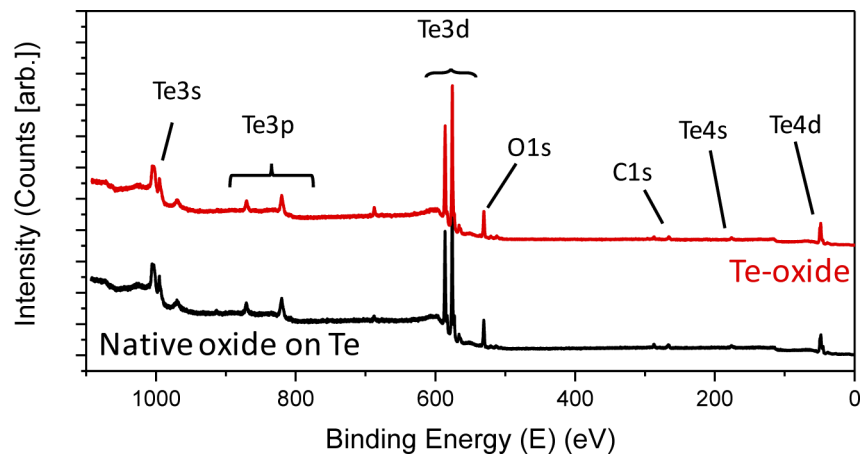


Fig. 3. Wide scans of sample TeO and Native oxide on Te. The spectra were charge-corrected to the unoxidized $\text{Te}3d_{5/2}$ core level peak at 573 eV.

The stoichiometry of the Te-oxide for both samples are quantified from Eq. (1) by extracting the atomic concentration of the normalized peak areas of the oxidized $\text{Te}3d_{5/2}$ peak with respect to the O1s normalized peak area,

$$\text{At}\% \text{ of } \text{Te}3d_{5/2}(\text{oxide}) = \frac{\frac{\text{Peak area of } \text{Te}3d_{5/2}(\text{oxide})}{SF(\text{Te}3d_{5/2})}}{\frac{\text{Peak area of } \text{Te}3d_{5/2}(\text{oxide})}{SF(\text{Te}3d_{5/2})} + \frac{\text{Peak area of } \text{O}1s}{SF(\text{O}1s)}} \times 100\% \quad (1)$$

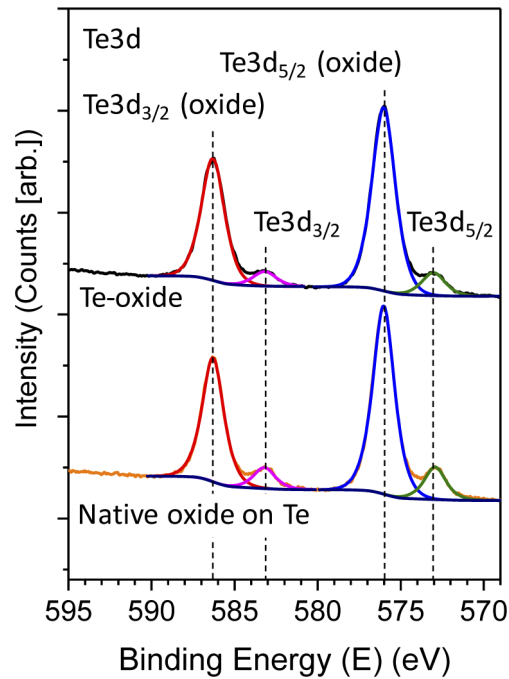


Fig. 4. Te3d core-level spectra for samples TeO and native oxide on Te. The spectra show the presence of unoxidized Te and oxide Te in the form of TeO_x where $x \sim 1.2$.

where SF is the Sensitivity Factor for each respective core-level peak. The At% concentrations for $\text{Te3d}_{5/2}$ oxide and O1s are shown in Table 1. For both samples TeO and native oxide on Te, the ratio of the At% concentration of Te to that of O1s is approximately 1:1.2, suggesting that these samples contain sub-oxide TeO_x where $x \sim 1.2$.

Table 1. Concentrations (At%) of $\text{Te3d}_{5/2}$ (oxide) and O1s and their (At%) ratio for sample TeO and native oxide on Te. For both samples, the ratio values show that the stoichiometry of Te-oxide is TeO_x where $x \sim 1.2$.

Sample	Core-level peak	Peak BE (eV)	FWHM (eV)	At. %	Ratio (Te:O)
TeO	$\text{Te3d}_{5/2}$ (oxide)	576.0	1.6	45.8	1 : 1.2
	O1s	530.8	2.0	54.2	
Nat. oxi. on Te	$\text{Te3d}_{5/2}$ (oxide)	576.0	1.7	45.5	1 : 1.2
	O1s	530.8	2.0	54.5	

Even though the Te:O ratio was found to be slightly different from 1:1, for simplicity we express $\text{Te}_1\text{O}_{1.2}$ as TeO or TeO_x throughout the text. In view of similarities of both X-ray spectra, and neglecting the possibility of a stoichiometry gradient, hereinafter the optical constants of TeO will be used to model the native oxide growth on Te in the models. Fig. 5 depicts XRR experimental measurements on Te and TeO samples, and the respective models. Once we have modelled the substrate, incident polarization, and the TeO and native oxide stoichiometries, the parameters obtained from XRR are film density, thickness, and surface/interface root mean square (R_q) roughness. Additionally, for Te films, the thickness of the native oxide, modelled as TeO, is also retrieved. The parameters obtained from the models are shown in Table 2, under XRR columns. Possible interfaces between Substrate-Te and Substrate-TeO have not been considered, neither density nor stoichiometry gradients within films.

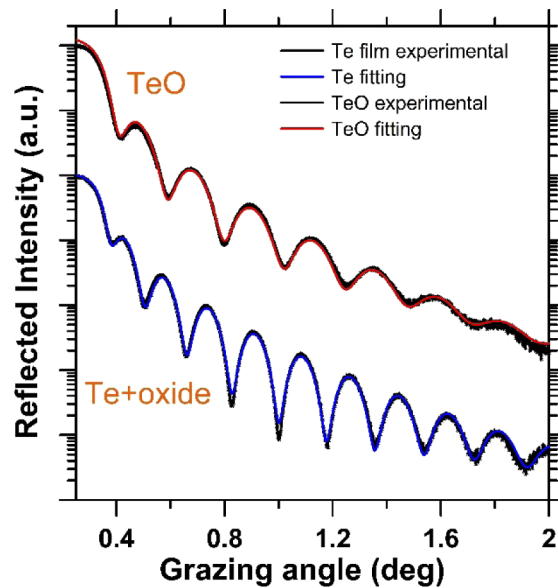


Fig. 5. XRR of Te (with native oxide) and TeO samples deposited on quartz and their models, in logarithm scale.

Table 2. Parameters obtained from the fittings.

Sample	Thickness (nm)		Density (g/cm ³)		Roughness, Rq (nm)	
	XRR	EUV R	XRR	EUV R	XRR	EUV R
TeO	18.3	18.5	5.830	-	0.34	0.72
Sample	Thickness (nm)		Density (g/cm ³)		Roughness, Rq (nm)	
	XRR	EUV R	XRR	EUV R	XRR	EUV R
Native oxide	2.7	2.3	5.881	-	0.21	0.88
Te	20.7	21.1	6.154	-	0.17	0.41

The density of Te film was found to be 6.154 g/cm³, which is 98.6% of its bulk density (6.24 g/cm³). This high density is somehow expected as PLD produces very dense films even if deposited at room temperature, as the high energy of incident particles (several dozens of eV) greatly enhances adatoms mobility on the substrate's surface. The density of TeO and of the native oxide growth on top of Te was found to be 5.830 g/cm³ and 5.881 g/cm³, respectively, which are quite similar; this similarity is in good agreement to what it has been shown through XPS analysis. No information was found in the literature about the density of TeO; as a reference, TeO₂ tabulated density is 5.67 g/cm³.

Figures 6(a) and 7(a) display reflectivity versus incident angle of TeO and Te films in the range 13-14 nm, with 0.1 nm step. For clarity, reflectance curves and models are multiplied for a factor of 2 with respect to the previous wavelength, starting from the curves at 13 nm which are multiplied by 2⁰; hence, curves of 13.1 nm are multiplied by 2¹, curves of 13.2 are multiplied by 2² and so forth, until curves of 14 nm which are multiplied by a factor 2¹⁰. The fitting range was from 87 degrees to 7 degrees. Measurements below 7 degrees are expected to differ from experimental data because the beam is partially blocked by sample (at zero degrees, the beam section is half-cut by the sample). Above 87 degrees, the detector partially blocks the incoming photon beam. The absorbing properties of both Te and TeO films are evident at a first glance, as the amplitude of the oscillations in the reflectivity measurements displayed in Figs. 6(a) and 7(a)

are small. These oscillations are produced by interference effects between the sample interfaces due to the finite thickness of films. As they are very absorbent, the interference is weaker (most of the photons transmitted through the first interface and reflected in the second interface are absorbed) and therefore the oscillation amplitude is smaller than what would be seen in more transparent films with the same thickness, for instance, in Silicon. At this point we have a better knowledge about Te and TeO samples from previous experiments. Thus, parameters obtained in previous analyses were either fixed or allowed for small variations in the fittings to determine the optical constants. [18] As shown in Figs. 6(a) and 7(a), there is an excellent agreement between models and experimental data for both Te and TeO samples. Model parameters for EUV reflectance measurements on Te and TeO samples are included in Table 2 under “EUV R” columns. There are significant differences between the roughness values obtained XRR and through the EUV reflectivity fittings. One possible explanation for this mismatch is that different spatial frequencies of roughness play a fundamental role in either XRR or EUV measurements. XRR measurements are more sensible to high spatial frequencies in roughness than EUV data, and usually the contribution of high spatial frequencies to roughness is smaller than the contribution of low frequencies. [19]

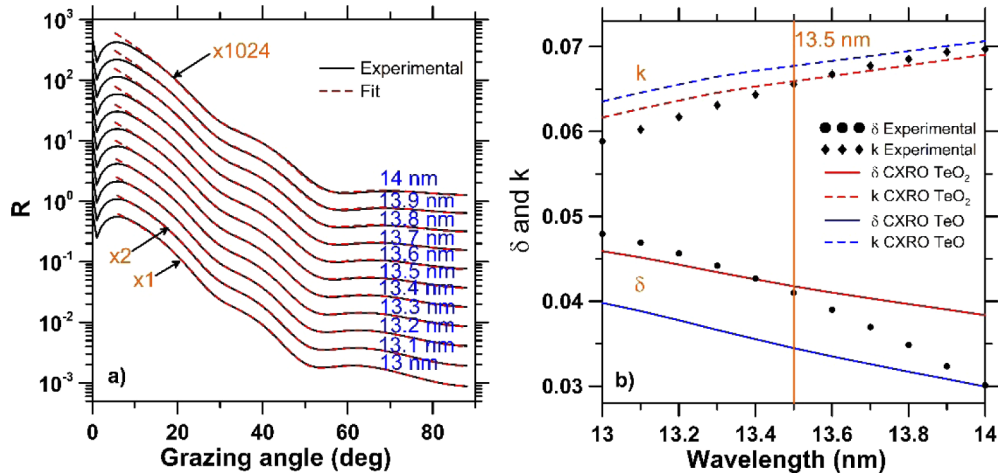


Fig. 6. a) Reflectance of TeO on quartz substrate as a function of the incident angle in the 13-14 nm with 0.1 nm step. Note that reflectances are multiplied by a factor 2^n for clarity. b) Experimental values of δ and k , compared with those of TeO and TeO₂ obtained through the tabulated atomic scattering factors⁴.

Figures 6(b) and 7(b) show the optical constants δ and k obtained from the fittings, along with tabulated data. For TeO, experimental optical constants are compared with those of TeO and TeO₂. As expected, there is some disagreement between the tabulated and calculated data as the independent atom approximation used in the calculation of the atomic scattering factors no longer applies in the vicinity of the Te N_{2,3} absorption edge. The calculated values of the optical constants at 13.5 nm are $\delta=0.03120$, $k=0.07338$ for Te, and $\delta=0.04099$, $k=0.06555$ for TeO. As a reference, the optical constants of TaN and TaBN at the same wavelength are $\delta=0.07401$, $k=0.04363$, and $\delta=0.04877$, $k=0.03265$, respectively. In comparison with TaN, Te and TeO present significantly larger k values, so that a similar low reflectivity could be achieved with a thinner absorber layer. Additionally, TeO and Te present δ values closer to unity, which would significantly reduce the index contrast with the free space and hence reduce the phase jump in the reflected wavefront at the edges of the patterned absorber. We have not evaluated the quality of the δ , k values, nor computed the error bars. Te and TeO optical constants have been

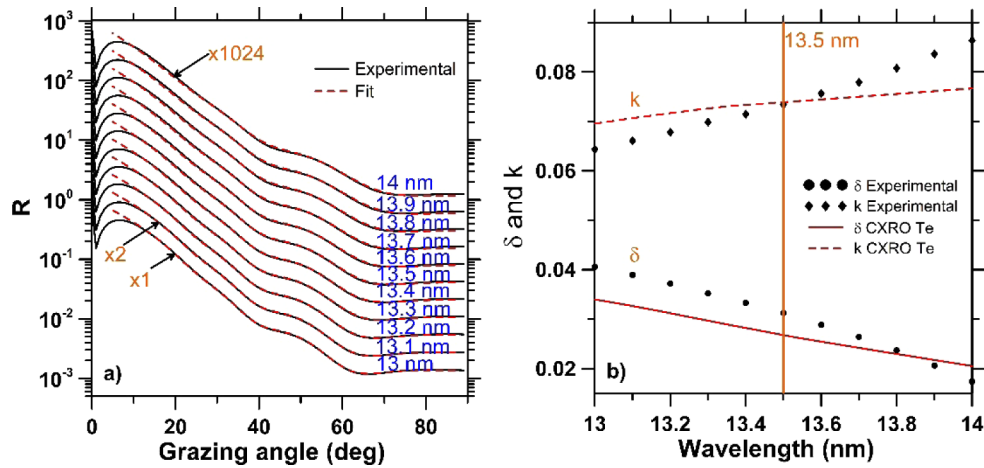


Fig. 7. a) Reflectance of Te on quartz substrate as a function of the incident angle in the 13-14 nm with 0.1 nm step. Note that reflectances are multiplied by a factor 2^n for clarity. b) Experimental values of δ and k , compared with those of Te obtained through the tabulated atomic scattering factors⁴.

calculated in the 13-14 nm range, which is ample enough for the intended application, but is not long enough to enable optical constant evaluation through sum-rules, which usually require δ , k values extended over a large portion of the electromagnetic spectrum. Moreover, the computation of reliable and traceable uncertainties is highly non-trivial (see for instance Gottwald *et al.* [20]).

4. Te and TeO absorbing properties on Mo/Si multilayers

The absorbing properties of Te and TeO were tested. A state-of-the-art mask-quality Mo/Si-based ML deposited on a large area Si wafer was cut in five different portions of around 10 mm x 10 mm size. One cut was left uncoated as a reference, whereas two portions were coated with different thicknesses of Te and the last two cuts were coated with different thicknesses of TeO. The deposition procedure was the same as described in subsection 2. Nominal thicknesses of Te and TeO absorber layers were selected as 2λ and $2\frac{1}{2}\lambda$ for both samples, which correspond to ~ 26.5 nm and ~ 33.5 nm for Te, and ~ 26.7 nm and ~ 33.7 nm for TeO, respectively. With this thickness selection, an additional reflectance reduction at 13.5 nm is expected due to interference effects (assuming $n \sim 1$), as is shown in Fig. 8. In the latter, the reflectivity curve of the bare ML was modelled beforehand, and then, on top of the ML a single absorber layer was added. The optical constants at 13.5 nm presented in Figs 6(b) and 7(b) were used for TeO and Te films, respectively. In Te films, the top 2.5 nm was considered to be TeO to model the native oxide. As for TaN, the optical constants were computed from the atomic scattering factors⁴ using a density of 16.3 g/cm^3 . Note that the typical TaN thickness to reduce ML reflectivity below 2% is larger than 50 nm, therefore the calculated TaN optical constants might be optimistic, as Fig. 8 indicates that a reflectivity $\sim 2\%$ could be achieved with only 42 nm of TaN.

Figures 9 and 10 show the absorption properties of Te and TeO films in the 13-14 nm range. The reflectivity of the uncoated reference ML is displayed in the same plot as reference. All reflectivity measurements were done at 6 degrees from normal incidence. Between coating and optical characterization, samples were stored few days in a controlled humidity and temperature cabinet.

Reflectivity at 13.5 nm for all samples displayed above are shown in Table 3. The nominal and real thicknesses of the absorber layers are also shown in Table 3. The real absorber thicknesses

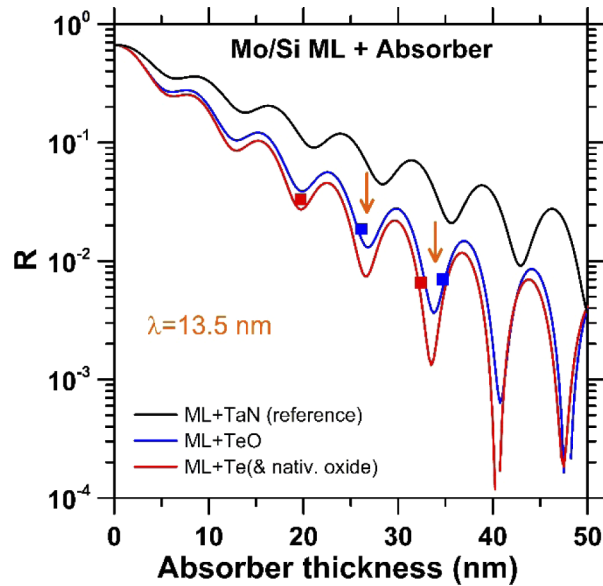


Fig. 8. Simulated reflectivity at 13.5 nm of a Mo/Si ML as a function of Te, TeO, or TaN absorber thicknesses, on a logarithmic scale. Interference effects yielding local reflectivity minima can be seen at optical thicknesses multiple of $\lambda/2$. The orange arrows indicate the intended thicknesses for both Te and TeO absorbers. Experimental values displayed in Table 3 are also included as filled squares.

Table 3. Reflectivity of samples as at 13.5 nm, along with the absorber thickness.

Sample	Nominal Absorber Thickness (nm)	Real Absorber Thickness (nm)	Measured R at 13.5 nm	Rq (nm)
Bare ML	-	-	66.7%	0.25
ML + Te(thin)	26.5	19.7	3.32%	1.02
ML + Te(thick)	33.5	32.4	0.66%	1.12
ML + TeO(thin)	26.7	26.1	1.87%	0.33
ML + TeO(thick)	33.7	34.7	0.70%	0.36

were obtained by fitting the reflectivity curves with the optical constants reported in the previous section. There is a good agreement between the real deposited TeO thicknesses and the intended values. However, for the thinner Te film there is a significant difference, which is attributed to miscalculations on the effect of the Te metallic layer that grew on the PLD laser entry window during the previous deposition. This coating significantly reduces the laser power delivered at the target's surface, and hence, modifies the deposition rate.

Considering the reflectivity versus absorber thicknesses curves displayed in Fig. 8, to obtain a reflectivity of around 0.7% using TaN as absorber the thickness should be around 50 nm, whereas we achieve a similar value with a thickness of 34.7 nm (TeO) or a thickness of 32.4 nm (Te). These values are thick enough to provide a good absorption, while thin enough to reduce the shadowing effects produced by 6-degrees illumination. The RMS roughness of the uncapped ML, and of different cuts of the same ML capped with either Te or TeO was measured with AFM. Absorbers should have a surface roughness below 0.5 nm so that the dimensional accuracy of the absorber pattern will not be degraded by the effect of roughness⁷. Figure 11 shows the topography of the uncapped ML (a), of the ML capped with the thinnest (b) and thicker (c) Te

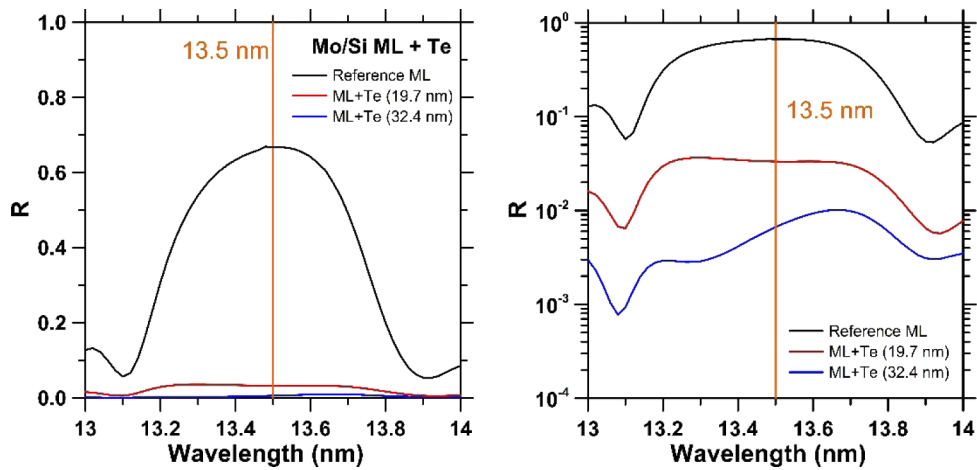


Fig. 9. Reflectivity vs wavelength of the reference Mo/Si ML (black), along with the same ML capped with 19.7 nm (red) and 32.4 nm (blue) of Te represented in both lineal and logarithm scales.

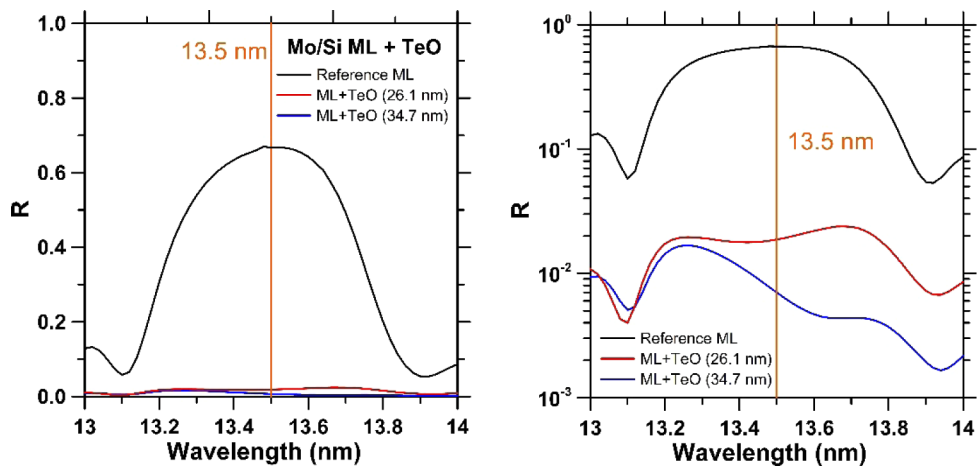


Fig. 10. Reflectivity vs wavelength of the reference Mo/Si ML (black), along with the same ML capped with 26.1 nm (red) and 34.7 nm (blue) of TeO represented in both lineal and logarithm scales.

layers, and of the ML capped with the thinnest (d) and thicker (e) TeO layers. Note the differences in the color scale. The resulting R_q values are displayed in Table 3.

The high R_q values and the large grain sizes obtained on Te-capped MLs invalidate its use as absorber. Although the high surface roughness of Te-capped MLs helps to reduce the reflectivity (in fact, using the well-known Debye [21] and Waller [22] equation, 1-nm roughness at 13.5 nm wavelength may reduce reflectivity by $\sim 1\%$), it happens at the expense of increasing scattered light, which is an undesired effect as it may affect the quality of the projected patterns. On the other hand, both TeO-capped MLs present R_q values of 0.33 and 0.36 nm for the thin and thicker layers respectively, which are acceptable ($R_q \approx \lambda/40$). AFM images also indicate a fine polycrystalline morphology on TeO-capped MLs, which is desirable for absorbers.

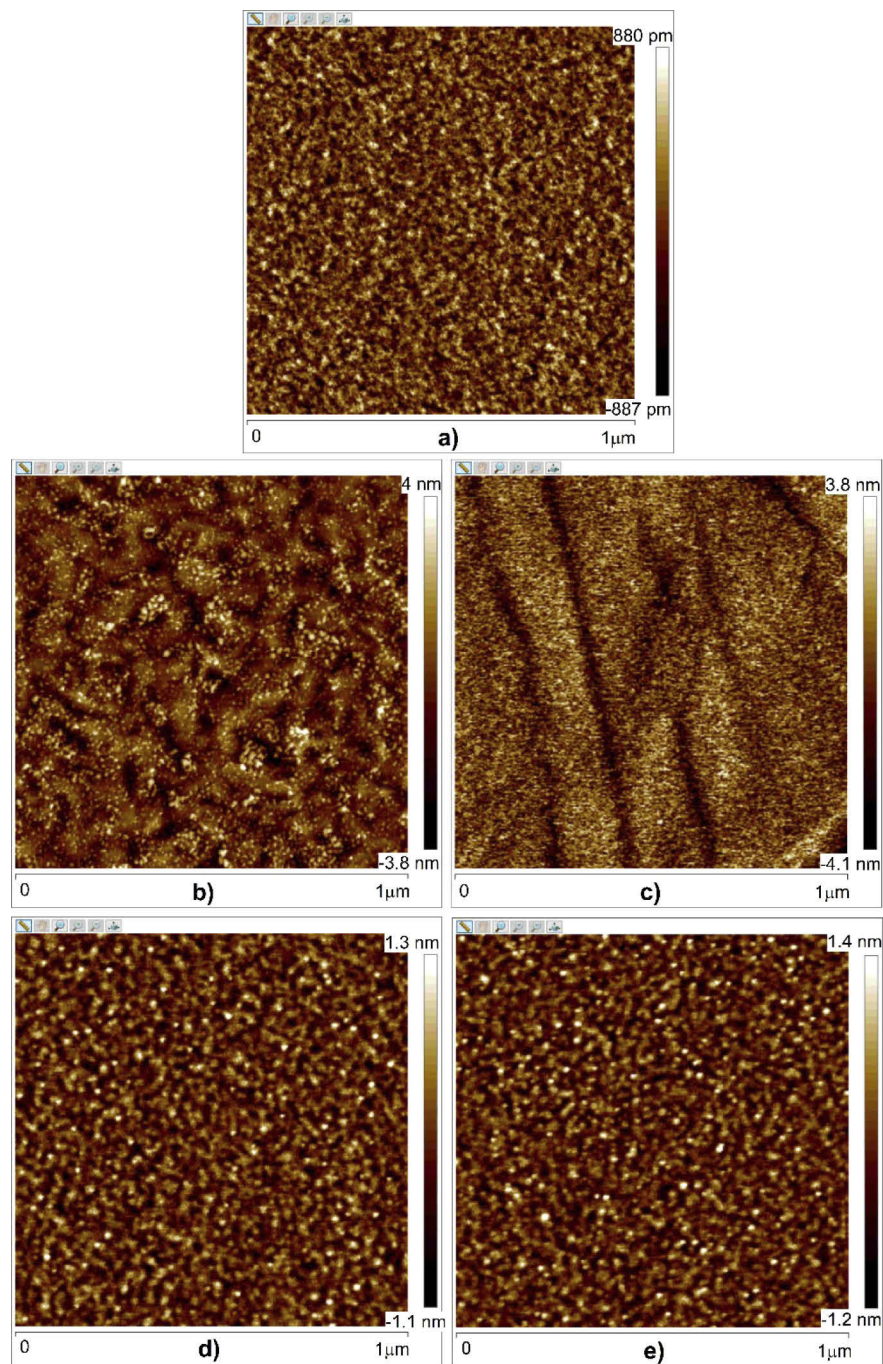


Fig. 11. Topography of the reference ML (a), of the Te-capped MLs (b: thin Te, c: thick Te), and of the TeO-capped MLs (d: thin TeO, e: thick TeO). The base ML is the same for all samples. Note that Z scales are different in each picture.

5. Conclusions

In this work we have explored the use of Te and TeO thin films as potential absorbers for reflective EUVL masks operating at 13.5 nm. Hence, the optical properties (δ and k) of Te and TeO films are calculated in the 13-14 nm range with 0.1 nm step. δ and k are obtained via models that fit experimental values of EUV reflectivity vs angle of incidence. To improve the accuracy of the data, several characterization techniques have been combined to fix and reduce the number of fitting parameters. At 13.5 nm, Te presents $\delta=0.03120$, $k = 0.07338$, whereas TeO presents $\delta=0.04099$, $k = 0.06555$. Hence, at 13.5 nm Te is found to be more absorbent than TeO and has a smaller δ value (or its $n = 1-\delta$ is closer to unity). The absorbing properties of Te and TeO films are tested on a EUV mask-quality Mo/Si ML. 19.7 nm and 32.4 nm of Te produce a reflectivity drop at 13.5 nm from 66.7% (the reflectivity of the uncapped ML) to 3.32% and 0.66%, respectively, whereas TeO layers of 26.1 nm and 34.7 nm decrease the reflectivity of the same ML down to 1.87% and 0.70%, respectively. TaN absorbers require around 50 nm to reduce reflectivity below 2%, whereas only 26.1 nm of TeO yields a similar reduction. AFM measurements on MLs capped with TeO show a fine polycrystalline morphology along with acceptable (<0.5 nm) roughness values of 0.33 nm and 0.36 nm for the thinnest and thickest TeO layers, respectively. The same ML capped with Te films present R_q roughness values above 1 nm, along with a coarse grain morphology.

Ignoring some fundamental properties that an absorber should meet which have not been explored in this work, we show that TeO is a potential candidate to replace TaN as an absorber for EUVL photomasks operating at 13.5 nm.

Funding

National Research Foundation Singapore (R-398-000-087-281); Ministry of Education - Singapore (R-144-000-379-114, R-144-000-423-114); Ministry of Education - Singapore (MOE2017-T2-1-135, MOE2018-T2-2-117).

Acknowledgments

We thank Weimin Li and Chen K. Wui for the invaluable help with EUV measurements and AFM data. We also thank Xiaojian Yu for his assistance and troubleshooting guidance with SINS and EUV branch beamline. We thank Yang Ping for his assistance with measurements with XDD beamline. The authors would also like to acknowledge the Singapore Synchrotron Light Source (SSLS) for providing the facility necessary for conducting the research. The Laboratory is a National Research Infrastructure under the National Research Foundation in Singapore.

Disclosures

The authors declare no conflicts of interest.

References

1. G. McIntyre, C. S. Koay, M. Burkhardt, H. Mizuno, and O. R. Wood II, "Modeling and experiments of non-telecentric thick mask effects for EUV lithography," *Proc. SPIE* **7271**, 72711C (2009).
2. V. Philipson, K. V. Luong, L. Souriau, A. Erdmann, D. Xu, P. Evanschitzky, R. W. E. van de Kruijs, A. Edrisi, F. Scholze, C. Laubis, M. Irmscher, S. Naasz, C. Reuter, and E. Hendrickx, "Reducing extreme ultraviolet mask three-dimensional effects by alternative metal absorbers," *J. Micro/Nanolith. MEMS MOEMS* **16**(4), 041002 (2017).
3. N. Fui, Y. Liu, X. Ma, and Z. Chen, "EUV Lithography: State-of-the-Art Review," *J. Microelectron. Manuf.* **2**(2), 1-6 (2019).
4. B. L. Henke, E. M. Gullikson, and J. C. Davis, "X-ray interactions: photoabsorption, scattering, transmission, and reflection at $E = 50-30000$ eV, $Z = 1-92$," *At. Data Nucl. Data Tables* **54**(2), 181-342 (1993).
5. T. Matsuo, K. Kanayama, and Y. Okumoto, "Novel absorber materials for EUV lithography mask," *Proc. SPIE* **7379**, 73792G (2009).

6. V. Philipsen, K. V. Luong, L. Souriau, E. Altamirano-Sánchez, C. Adelman, C. Laubis, F. Scholtze, J. Kruemberg, C. Reuter, and E. Hendrickx, "Single element and metal alloy novel EUV mask absorbers for improved imaging," *Proc. SPIE* **10450**, 104500G (2017).
7. P. Yan, G. Zhang, P. Kofron, J. E. Powers, M. Tran, T. Liang, A. R. Stivers, and F. Lo, "EUV mask absorber characterization and selection," *Proc. SPIE* **4066**, 116–123 (2000).
8. O. Wood II, S. Raghunathan, P. Mangat, V. Philipsen, V. Luong, P. Kearney, E. Verduijn, A. Kumar, S. Patil, C. Laubis, V. Soltwisch, and F. Scholze, "Alternative materials for high numerical aperture extreme ultraviolet lithography mask stacks," *Proc. SPIE* **9422**, 94220I (2015).
9. B. La Fontaine, A. R. Pawloski, Y. Deng, C. Chovino, L. Dieu, O. R. Wood II, and H. J. Levinson, "Architectural choices for EUV lithography masks: patterned absorbers and patterned reflectors," *Proc. SPIE* **5374**, 300–310 (2004).
10. R. Fallica, J. Haitjema, L. Wu, S. Castellanos-Ortega, A. M. Brouwer, and Y. Ekinici, "Absorption coefficient of metal-containing photoresist in the extreme ultraviolet," *J. Micro/Nanolith. MEMS MOEMS* **17**(2), 023505 (2018).
11. V. Philipsen, K. V. Luong, K. Opsomer, C. Detavernier, E. Hendrickx, A. Erdmann, P. Evanschitzky, R. W. E. van de Kruijs, Z. Heidarnia-Fathabad, F. Scholze, and C. Laubis, "Novel EUV mask absorber evaluation in support of next-generation EUV imaging," *Proc. SPIE* **10810**, 108100C (2018).
12. H. Y. Kang, P. Peranatham, and C. K. Hwangbo, "Optical properties of TaTe2O7 thin films as absorber materials for extreme ultraviolet lithography binary masks," *J. Vac. Sci. Technol., B: Nanotechnol. Microelectron.: Mater., Process., Meas., Phenom.* **30**(6), 06F505 (2012).
13. R. Soufli, Optical constants of materials in the EUV/soft x-ray region for multilayer mirror applications, PhD Thesis, (University of California, 1997).
14. X. Yu, C. Diao, T. Venkatesan, M. B. H. Breese, and A. Rusydi, "A soft x-ray-ultraviolet (SUV) beamline and diffractometer for resonant elastic scattering and ultraviolet-vacuum ultraviolet reflectance at the Singapore synchrotron light source," *Rev. Sci. Instrum.* **89**(11), 113113 (2018).
15. <http://ssls.nus.edu.sg/facility/xdd.html>
16. N. F. Brimhall, A. B. Grigg, R. S. Turley, and D. D. Allred, "Thorium dioxide thin films in the extreme ultraviolet," *Proc. SPIE* **6317**, 631710 (2006).
17. E. Palik, *Handbook of Optical Constants of Solids*, (Academic Press, 1985).
18. L. J. Bissell, D. D. Allred, R. S. Turley, W. R. Evans, and J. E. Johnson, "Determining ruthenium's optical constants in the spectral range 11-14 nm," *Proc. SPIE* **5538**, 84–91 (2004).
19. Chapter 2 in J. C. Stover, *Optical Scattering: Measurements and Analysis*, 3rd Edition (SPIE Press, 2012).
20. A. Gottwald, K. Wiese, U. Kroth, and M. Richter, "Uncertainty analysis for the determination of B4C optical constants by angle-dependent reflectance measurement for 40 nm to 80 nm wavelength," *Appl. Opt.* **56**(20), 5768–5774 (2017).
21. P. Debye, "Über der Intensitätsverteilung in den mit Röntgenstrahlung erzeugten Interferenzbildern," *Verh. d. Deutsch. Phys. Ges.* **15**, 738 (1913).
22. I. Waller, "Zur Frage der Einwirkung der Wärmebewegung auf die Interferenz von Röntgenstrahlen," *Eur. Phys. J. A* **17**(1), 398–408 (1923).